Enhancing the performance of 3D porous N-doped carbon in oxygen reduction reaction and supercapacitor via boosting the meso-macropore interconnectivity using the “exsolved” dual-template

Ng, W.; Yang, Y.; van der Veen, K.; Rothenberg, G.; Yan, N.

DOI
10.1016/j.carbon.2017.12.019

Publication date
2018

Document Version
Final published version

Published in
Carbon

Carbon 129 (2018) 293–300

Contents lists available at ScienceDirect

Carbon

journal homepage: www.elsevier.com/locate/carbon

Enhancing the performance of 3D porous N-doped carbon in oxygen reduction reaction and supercapacitor via boosting the meso-macropore interconnectivity using the “exsolved” dual-template

Wesley Ng [a, 1], Ying Yang [b, 1], Koen van der Veen [a], Gadi Rothenberg [a], Ning Yan [a, *]

[a] Van't Hoff Institute for Molecular Sciences (HIMS), University of Amsterdam, Science Park 904, 1098 XH, Amsterdam, The Netherlands
[b] Department of Mechanics and Engineering Structure, Wuhan University of Technology, No.22 Luoshi Road, 430070, Wuhan, Hubei, China

ARTICLE INFO

Article history:
Received 11 October 2017
Received in revised form
5 December 2017
Accepted 6 December 2017
Available online 7 December 2017

Keywords:
In-situ exsolution
Hierarchically porous carbon
Pore connectivity
Oxygen reduction
Supercapacitor

ABSTRACT

The rational design and preparation of hierarchically porous carbons feature high on the wish list of academia and industry alike. However, creating interconnected pores of distinct dimensions is no easy task. Starting from the precursor design, we present a novel synthesis strategy of porous carbons that much enhances the pore interconnectivity. The 500 °C pyrolysis of chelated Mg and Fe nitrilotriacetates creates Fe-doped MgO template, sizing 50–400 nm. While embedded in the carbon matrix, these pyrolysis-generated templates undergo an additional phase transformation at the sequential 900 °C pyrolysis, exsolving well-dispersed smaller Fe nanoparticles, typically sizing 5–45 nm, on the MgO surface. This offers a contiguous network of dual templates for meso- and macropores. A simple acid washing yields a hierarchically porous, N-doped carbon with a high specific surface area of 1560 $m^2 g^{-1}$ and a high mesopore volume of 1.9 $cm^3 g^{-1}$. This carbon exhibits a half-wave potential of 0.77 V vs. RHE in the oxygen reduction reaction at pH 13. Besides, it also renders a specific capacitance of 321 F g^{-1} at 5 mV s^{-1} during the capacitor measurement.

1. Introduction

Functional materials are crucial for the advancement of science and technology, shaping our modern society. Porous carbon is a typical example. It contains pores and voids of controllable sizes and functionalities. This allows the interaction with the atoms and molecules not only at the surface, but also throughout the bulk of the material. Today, it is extensively used in real-life applications, such as when involving adsorption and catalytic processes [1–4].

Ideally, the classical micro- or meso-porous carbons have uniform pore dimensions and well-defined topologies, which is especially beneficial in the molecular separation [5]. In comparison, hierarchically porous carbon (HPC) comprises pores of more than one length scale. More importantly, these pores must be organized in such a way to be interconnected and freely accessible [6–8]. Hence, the smaller micropores create abundant active sites while simultaneously the larger meso- and macropores ensure rapid mass transfer. This complementarity is particularly favoured in the emerging energy conversion and storage technologies, enhancing the performance of fuel cells, supercapacitors, and Li-ion batteries [9–16].

Nonetheless, one of the major concerns regarding the development of HPC arises from the interconnectivity among the micro-, meso- and macropores [6,14,17,18]. The soft-templating method often requires expensive surfactants and polymers; its synthesis, consisted of gelation, solvent exchange and drying, is also time-consuming and complex. Alternatively, hard-templating approach often uses the externally added inorganic templates [6,8–10,14,15]. To generate hierarchical porosity and precisely manipulate the pore size, templates of different dimensions must be added to the carbon precursor. Nevertheless, it doesn't always guarantee a network with “all-connected-pores”. This becomes even more challenging when both high surface area and large pore volume are desired [3,6]. For example, the so-called “dual-templating” method uses templates of two sizes, which offers the manipulation of the pore scale and thus naturally gives pore hierarchy [4,15]. Yet the control of the meso-macropore interconnectivity is not perfect. Therefore, a rational synthesis of HPCs that creates “all-connected” pore networks remains a tough challenge.

* Corresponding author.
E-mail address: n.yan@uva.nl (N. Yan).
[1] These authors contribute equally to this work.

https://doi.org/10.1016/j.carbon.2017.12.019

Inspired by the recent studies on nanoparticle exsolution from perovskite oxides [19,20], we demonstrate here a rational yet facile approach for preparing HPCs. Aiming at increasing the electrochemical performances of the carbon, we promote the meso-macropore interconnectivity using a novel "exsolution" templating method. In this optimized hard-templating approach, the mesopore-template was exsolved from the previously formed macropore-template, naturally creating a connected network of template with dual dimensions. The design of the precursor and the structure evolution of the template are detailed. The composition, porous topology and the electrocatalytic performances of the HPCs are also discussed.

2. Experimental

2.1. Materials preparations

The electrocatalyst was prepared in a Teflon-lined stainless steel autoclave using the classical hydrothermal synthesis method. Initially, 2.5 mmol of nitrilotriacetic acid (NTA) ($N(CH_2COOH)_3$) was mixed with 1.5 mmol of magnesium carbonate and 0.25 mmol of iron acetate ($Fe(C_2H_3O_2)_2$) in 50 ml of de-ionized (DI) water. The molar ratio of NTA: Mg: Fe was 1:0.6:0.1. After thorough mixing, the suspension was then transferred to the autoclave (total capacity: 75 ml) for a 6 h reaction at 180 °C. Sequentially, the precipitate was obtained via centrifuging at 2600 rpm for 15 min. The resulting powder, denoted as FeMg-NTA, was washed several times with DI water. Three sets of reaction were done to give sufficient yield. After drying at 80 °C for 6 h, fine FeMg-NTA powder was acquired.

In the step-wise pyrolysis step, approximately 1.5 g of FeMg-NTA powder was loaded in a quartz boat that was placed in a quartz tube. The furnace was first heated up to 500 °C at 10 °C min^{-1} and then maintained at the temperature for 1 h to facilitate the formation of the doped template, namely, $Mg_{0.86}Fe_{0.14}O$. Then, the temperature was increased to 900 °C at the same heating rate for the 1 h final carbonization and the exsolution of Fe nanoparticles from the MgO lattice. The obtained fine black powder was denoted as FeMg-900. Both pyrolysis steps were performed under argon (99.99% purity) atmosphere with the flow rate of 130 ml min^{-1}. FeMg-NTA was also calcined in air at 900 °C to study the Fe doping effect in MgO.

The acid washing step was employed by mixing *ca.* 300 mg of FeMg-900 with excess of 100 ml 0.5 M HCl solution in a beaker. The suspension was strongly agitated overnight with mild heating at 50 °C before retrieving the solid residual by the sequential filtration and DI water washing. This acid washing step was repeated three times to ensure all the iron and magnesium impurities were removed. The finally obtained carbon was denoted as FeMg-carbon. The controls, namely, KMg-carbon and Mn-carbon, were prepared using the same approach. KOH and Mn acetate were applied as the potassium and manganese precursors, respectively. The molar ratio of NTA: Mg: K was kept the same as 1:0.6:0.1. However, no in-situ nanoparticle exsolution was expected in this control sample.

2.2. Materials characterizations

X-Ray diffraction (XRD) patterns were obtained using a MiniFlex II diffractometer equipped with the CuK_α radiation. The X-ray tube was operated at 30 kV with a current of 5 mA. The Rietveld refinement was performed using the GSAS Rietveld Software.

Nitrogen adsorption isotherms were measured on a Thermo Scientific Surfer instrument at 77 K. The specific surface area was measured according to the Brunauer-Emmett-Teller (BET) method from the desorption isotherm in the relative pressure range between 0.001 and 0.2. Horváth–Kawazoe (HK) and Barrett–Joyner–Halenda (BJH) models were applied to study the micropore and mesopore size distributions, respectively. The examined relative-pressure regions were 0–0.35 and 0.3–0.99, respectively. Non-local density functional theory (NLDFT) was also employed to examine the pore size distribution below 50 nm. The total pore volume was estimated from the amount of N_2 adsorbed at the relative pressure of 0.95. The macropore characteristic was investigated using the Mercury intrusion porosimetry that was carried out on a CE Instruments Pascal 440 measuring up to 400 MPa. The test temperature was fixed at 25 °C. All samples were pretreated by drying in vacuum (1×10^{-3} mbar) for 3 h at 200 °C prior to the measurement. Raman spectrum was recorded using a Thermo Nicolet Almega XR confocal Raman microscope at a 532 nm laser wavelength.

Temperature-programmed reduction (H_2-TPR) was performed on a Thermo TPDRO-1100 instrument equipped with a thermal conductivity detector (TCD). 10–15 mg of the catalyst was loaded to the quartz tube reactor, and the measurement was carried out in a stream of 5% H_2 in N_2 (40 ml min^{-1}) with a heating rate of 10 K min^{-1}. Thermogravimetric analysis (TGA) coupled with differential scanning calorimetry (DSC) was performed using a NETZSCH Jupiter® STA 449F3. The temperature range was 30–900 °C under the air atmosphere with flow rate of 20 ml min^{-1} at a heating rate of 5 K min^{-1}.

Scanning electron microscope (SEM) was used to observe the morphology of the samples using FEI Verios 60 equipped with a STEM (scanning-transmission electron microscope) detector that enabled BF/DF/HAADF imaging. The acceleration voltage was 30 kV. Transmission electron microscope (TEM) analysis was also performed using a JEOL 2200 FS TEM. X-ray photoelectron spectroscopy (XPS) was carried out using a Kratos AXIS equipped with a monochromatic Al K_α X-ray source. The base pressure in the analytical chamber was maintained at 10^{-9} mbar. The obtained spectra were analyzed using the Thermo Avantage software calibrated to the C 1s binding energy of 285.0 eV. For curve fitting and deconvolution, a Shirley-type background subtraction and a Gaussian-Lorentzian peak shape were applied. In the assignment of nitrogen functionalities, we avoided using the pyrrolic, because they are known to decompose at temperatures above 800 °C to either pyridinic or graphitic nitrogen [21,22].

2.3. Electrochemical procedures

In the oxygen reduction reaction study, we used the standard rotating disc electrode (RDE) setup to evaluate the activity of the catalyst. Four catalyst inks were initially prepared in the experiments, consisting of commercial Pt/C (20 wt % Pt on Vulcan XC 72, fuel cell grade, Premetek, USA), FeMg-900, FeMg-carbon and KMg-carbon. In a typical preparation, 1 ml ethanol, 10 μL Nafion® (D-521 dispersion 5 wt % in water/isopropanol, Alfa Aesar 42117) and 1 mg catalyst powder were mixed in a vial and sonicated overnight.

Dropcasting was applied to prepare the glassy carbon RDE (Gamry, USA) with a diameter of 5 mm (A = 0.196 cm^2). First, the RDE was polished sequentially by diamond polishing films with 1 and 0.1 μm particles (Allied High Tech Products, USA) with water rinse. Inks were then dropcasted by 5 μL portion × 6, with air drying in between. The total catalyst loading was 30 μg, or 153 μg/cm^2.

Electrochemical experiments were performed in a classic 3-electrode setup. 0.1 M KOH solution, stabilized at 25.0 ± 0.1 °C in a water bath, was used as the electrolyte. A Gamry Reference 600 potentiostat was employed, together with a Gamry RDE710 rotating electrode setup. Saturated calomel electrode (SCE, Gamry, USA) separated from the solution by a 10 cm bridge was used as a reference electrode, and a graphite rod (Gamry, USA) as a counter

electrode. Potentials were reported vs. reversible hydrogen electrode (RHE) in all cases by adding 1.011 for pH 13. Nitrogen (99.999%) or oxygen (99.999%) were bubbled for 30 min to saturate the solution, and were flowed above the solution ('gas blanket') during the experiments. The solution resistance was determined initially, and 95% of the value (typically 30–50 Ω) was used as a positive correction factor in an automatic iR drop correction in the voltammetric measurements. The linear scan voltammograms (LSV) were obtained with a scan rate of 10 mV s^{-1} at rotating speeds of 400, 600, 900, 1200, 1600, 2000 and 2400 rpm. Cyclic voltammetry was measured with the same parameters but without rotation. Electrochemical impedance spectroscopy (EIS) was carried out in the range of 0.1-10^5 HZ at the half-wave potential of ORR with an AC perturbation of 10 mV.

2.4. Koutecký-Levich plots

The number of electrons transferred in the reaction was estimated by the Koutecký-Levich equation:

$$\frac{1}{J} = \frac{1}{B\omega^{1/2}} + \frac{1}{J_K}$$

where J is the measured current density (mA cm^{-2}), J_K is the kinetic (exchange) current density (mA cm^{-2}), ω is the RDE rotation rate (rpm), and B is given by:

$$B = 0.2nFC_O D_O^{2/3} \nu^{-1/6}$$

where 0.2 is the arithmetic correction factor for ω in rpm, n is the number of electrons transferred per mol, F is Faraday's constant, C_O is the concentration of dissolved O_2 (1.2 mmol ml^{-1} at 25 °C in 0.1 M KOH), D_O is the diffusion coefficient of O_2 (1.9×10^{-5} cm^2 s^{-1} at 25 °C in 0.1 M KOH), and υ is the kinematic viscosity of the 0.1 M KOH electrolyte at 25 °C (0.01 cm^2/s). By plotting $1/J$ versus $\omega^{-1/2}$ at different potentials and fitting linear equations to the data, the number of electrons (n) could be calculated from the slope ($1/B$).

2.5. Supercapacitor measurement

A typical 3-electrode setup was used to measure the capacitance. 1 M H_2SO_4 solution was used as the electrolyte whereas the SCE and a thick platinum wire were used as the reference and counter electrode, respectively. To prepare the working electrode, 10 mg of polyvinylidene fluoride (PVDF) was dissolved in 5 ml N-methyl-2-pyrrolidone (NMP), the overnight sonication resulted in the formation of a clear solution. Then 50 mg of the carbon materials (KMg-carbon and FeMg-carbon) were added to the solution to form the homogeneous slurry. It was then coated onto the 1 × 1 cm area of a gently pressed Ni foam (3 × 1 cm) that has been cleared by ethanol, 0.1 M HCl and water sequentially. After drying it in a vacuum oven at 80 °C for 3 h, the carbon loading (*ca.* 1 mg) was measured precisely by the balance.

In the electrochemical measurement, nitrogen was first bubbled for 15 min to saturate the solution. The cyclic voltammograms (CV) were attained at different scan rates in the potential range of −0.35–0.6 V (*vs.* SCE). The gravimetric capacitance was calculated from the CV plot using the *Echem Analyst* software according to the equation below:

$$C = \frac{S_{area}}{2m\nu\Delta V}$$

Where S_{area} was the integrated loop area of the voltammogram, m is the mass of the carbon on the Ni foam, v is the scan rate and ΔV is the voltage window.

3. Results and discussion

The precursor was prepared following our hydrothermal treatment method of nitrilotriacetic acid mixed with Mg and Fe salts of a 6:1 M ratio (FeMg-NTA) [23]. As NTA chelated with both Mg and Fe cations, the recovered solid presumably has a polymeric structure as we showed previously [9]. The step-wise pyrolysis started at 500 °C, delivering Fe doped MgO nanoparticles embedded in a partially carbonized polymer as illustrated in Fig. 1. Subsequently carbonizing this compound at 900 °C caused the exsolution of well-distributed small iron nanospheres that covered the larger MgO nanoparticles. The selection of 900 °C carbonization temperature was based on our previous experience [9,10], ensuring a high level of graphitization yet avoiding the formation of iron carbide. The Fe and MgO spheres thus served as the mesopore and the macropore templates, respectively. Washing away these embedded dual-templates with HCl yielded a hierarchically porous structure containing well-interconnected micro-, meso- and macropores (*cf.* the isolated meso/macro-pores in Fig. S1 using conventional approach).

The X-ray diffraction (XRD) patterns in Fig. 2a reveal the crystal structure evolution of the template. The 500 °C pyrolysis of FeMg-NTA gave a pure halite structure without iron impurities (FeMg-500) [24]. The formation of $Mg_{0.86}Fe_{0.14}O$ was also confirmed by the Rietveld refinement in Fig. 2b, with a 0.002 Å shrinkage of the cubic lattice to 4.210 Å. The (220) plane peak also shifted at *ca.* 62°. Interestingly, $Mg_{0.86}Fe_{0.14}O$ was not achievable via calcinating FeMg-NTA (iron oxides were evidenced by XRD, see Fig. S2). As the pyrolysis temperature increases to 900 °C, the strong reducing environment induced iron precipitation, exsolving Fe nanoparticles on the surface of MgO (FeMg-900). Temperature programmed reduction studies (H_2-TPR, Fig. S3) also supported this. After washing out the dual templates, the XRD pattern shows only carbon peaks (FeMg-carbon).

X-ray photoelectron spectroscopy (XPS) data reveals the chemical composition of the HPC. Remarkably, the resulting carbon had abundant intrinsic defects as demonstrated in the deconvoluted C1s core-level spectrum in Fig. 2c. The peak at 284.0 eV originated from the non-conjugated carbon atoms in the hexagonal lattice [25,26], which was assigned to carbon vacancies (sp^2 carbon, also see the comparison in Fig. S5). Other peaks at 284.8 eV, 285.7 eV, 286.6 eV and 289.0 eV were ascribed to graphitic carbon, C–OH, C–O–C and C=O, respectively [26]. No iron signal has been recorded in the measurement. However, the total nitrogen doping ratio was extremely low. The N 1s core-level spectrum in Fig. 2e was deconvoluted into pyridinic (398.8 eV), graphitic (400.7 eV) and oxidized (401.6 eV) nitrogen moieties. The ratio of pyridinic nitrogen, which has been recently shown as the key catalytic active site in oxygen reduction reaction, was 0.2%. This value is rather small compared with the literature and our control group (see Table S1 for details). In the Raman spectrum in Fig. 3, the presence of iron carbide was also ruled out, as iron impurity was not identified particularly below 900 cm^{-1} [16,26]. the strong peaks, denoted as D and G, represent the defect and graphitic carbon, respectively. We therefore conclude that the abundant intrinsic carbon defects are the main active sites that boost the oxygen reduction reaction performance as widely documented before [27–33].

We then investigated the morphologies of all samples. The transmission electron microscope (TEM) image of FeMg-500 in Fig. 4a shows the embedded $Mg_{0.86}Fe_{0.14}O$ particles in the carbon matrix, confirmed by the elemental mappings. The scanning electron microscope (SEM) analysis in Fig. 4b using backscattered electron imaging indicates that these templates, with heavier atomic weights and thus brighter color, remained homogenously

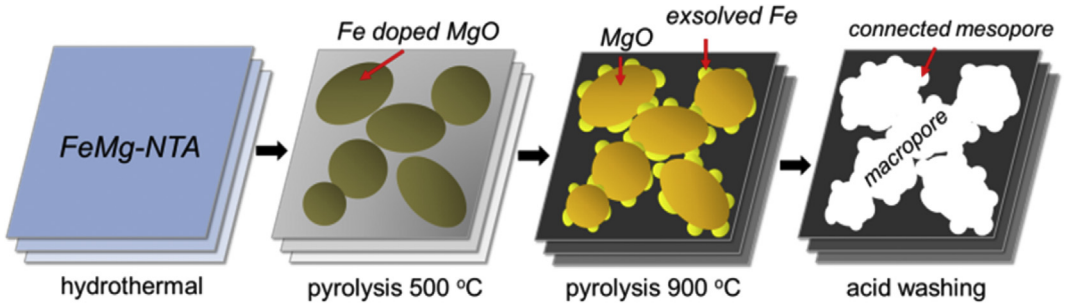

Fig. 1. The structural evolution of nitrilotriacetates during the two-step pyrolysis and the formation of hierarchical porous carbon. The transition metal cations sequentially form Fe-doped MgO and *in-situ* exsolved Fe nanoparticles on MgO, creating an interconnected template network for hierarchical pores. (A colour version of this figure can be viewed online.)

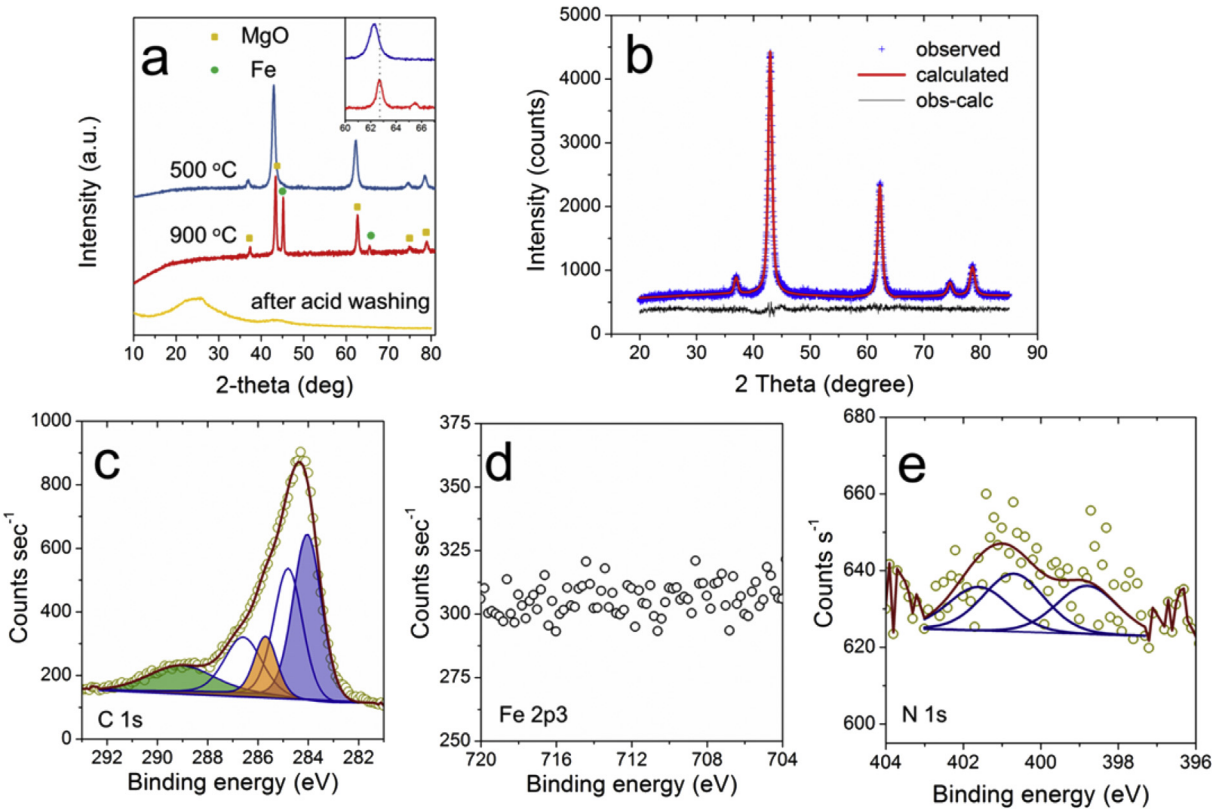

Fig. 2. (a) XRD patterns FeMg-500, FeMg-900 and FeMg-carbon; (b) Rietveld refined XRD pattern of FeMg-500. XPS spectra of (c) C 1s core-level, (d) Fe 2p3 core-level and (e) N 1s core-level of FeMg-carbon. (A colour version of this figure can be viewed online.)

distributed in FeMg-900. Their typical sizes were between 50 nm and 400 nm, well matching the scale of macropores. A high resolution SEM image in Fig. S6 clearly shows the exsolved iron species on the surface of MgO. Their dimensions spanned from 20 nm to 45 nm, falling into the right range of templating mesopores. The high resolution TEM (HRTEM) micrograph shows that the majority of iron compound are sized less than 20 nm: the inset of Fig. 4b demonstrates a typical precipitated Fe nanoparticle on MgO, both of which were encapsulated by graphitic carbon layers as they were capable of catalyzing graphitization [34,35]. This showed the effectiveness of our approach for templating interconnected hierarchical pores.

After acid washing, the FeMg-carbon material showed high porosity with no metallic inclusions, in good agreement with the XPS and Raman results. Notably, both mesopores and macropores, templated from the Fe and MgO nanoparticles respectively, are clearly seen in the HRTEM micrograph (Fig. 4d–e). They were densely packed and interconnected. The typical pore-wall thickness was below 5 nm, comparable with that of the graphitic layer in the inset of Fig. 4b. This supported our hypothesis that the pores originated from the templates. As micropores came from the etching effect of CO_2 during the pyrolysis, they were observable within both meso- and macropores [9].

To determine the pore characteristics of FeMg-carbon, we ran both N_2-adsorption/desorption and mercury intrusion porosimetry. A summarized physico-chemical properties comparison of FeMg-carbon and the control was shown in Table S1. Fig. 5a compares the adsorption/desorption isotherm of nitrogen on FeMg-carbon with a KMg-carbon control sample, which was also derived from nitrilotriacetate precursors. The FeMg-carbon sample has a specific surface area of 1560 $m^2\ g^{-1}$, comparable to that of the KMg-carbon (2047 $m^2\ g^{-1}$). But its total pore volume was much higher

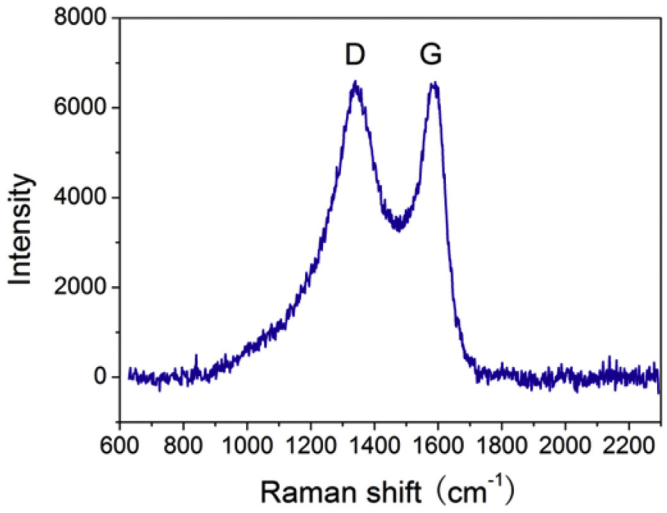

Fig. 3. Raman spectrum of FeMg-carbon. (A colour version of this figure can be viewed online.)

(2.7 $cm^3\ g^{-1}$ *vs.* 1.5 $cm^3\ g^{-1}$) thanks to the *in-situ* exsolved Fe templates. This value is higher than many porous carbons made by templating methods (see the detailed comparison in Ref. 6).

In fact, the FeMg-carbon sample demonstrated the combined features of the classical type I, II and IV isotherm, indicating the coexistence of micro-, meso- and macropores. Conversely, the isotherm of the KMg-carbon sample was closer to type I. The hysteresis loop, often results from the cavitation-controlled evaporation, also discloses key information about the pores. According to the IUPAC classification [36], the FeMg-carbon sample featured a combined H3 and H4 loop that was typical of micro-meso-macroporous materials. While the KMg-carbon sample also showed the H4 feature, the contribution of meso- and macropores was not prominent.

We then analyzed the pore size by calculating the micropore size distribution using the Horváth–Kawazoe (HK) model (Fig. 5b). Both materials had similar microporous features. The Barrett–Joyner–Halenda (BJH) calculation in Fig. 5c reveals the substantially higher mesopore density in FeMg-carbon, particularly in the 5–30 nm region, well matching the size of the exsolved Fe template. It should be pointed out that the "4-nm" mesopore peak is a common artifact in the N_2 adsorption measurement due to the sudden evaporation of liquid N_2 (see the abrupt drop in the desorption isotherm at 0.4 P/P^0). Both the mesopore surface area and volume were dramatically boosted (987 *vs.* 279 $m^2\ g^{-1}$; 1.9 *vs.* 0.5 $cm^3\ g^{-1}$). The same conclusion could be drawn from the NLDFT calculation in Fig. S7.

For studying the larger pores, we used Hg intrusion porosimetry. Fig. 5d compares the pore size distribution from 4 to 100 nm. Remarkably, FeMg-carbon was much more porous than the control, well matching the N_2-adsorption results in Fig. 5c. Its pore volume ($D < 207$ nm) tripled that of KMg-carbon (1.61 and 0.35 $cm^3\ g^{-1}$, respectively; the histogram comparing both materials is shown in Fig. S8). Note that these values were lower than those obtained

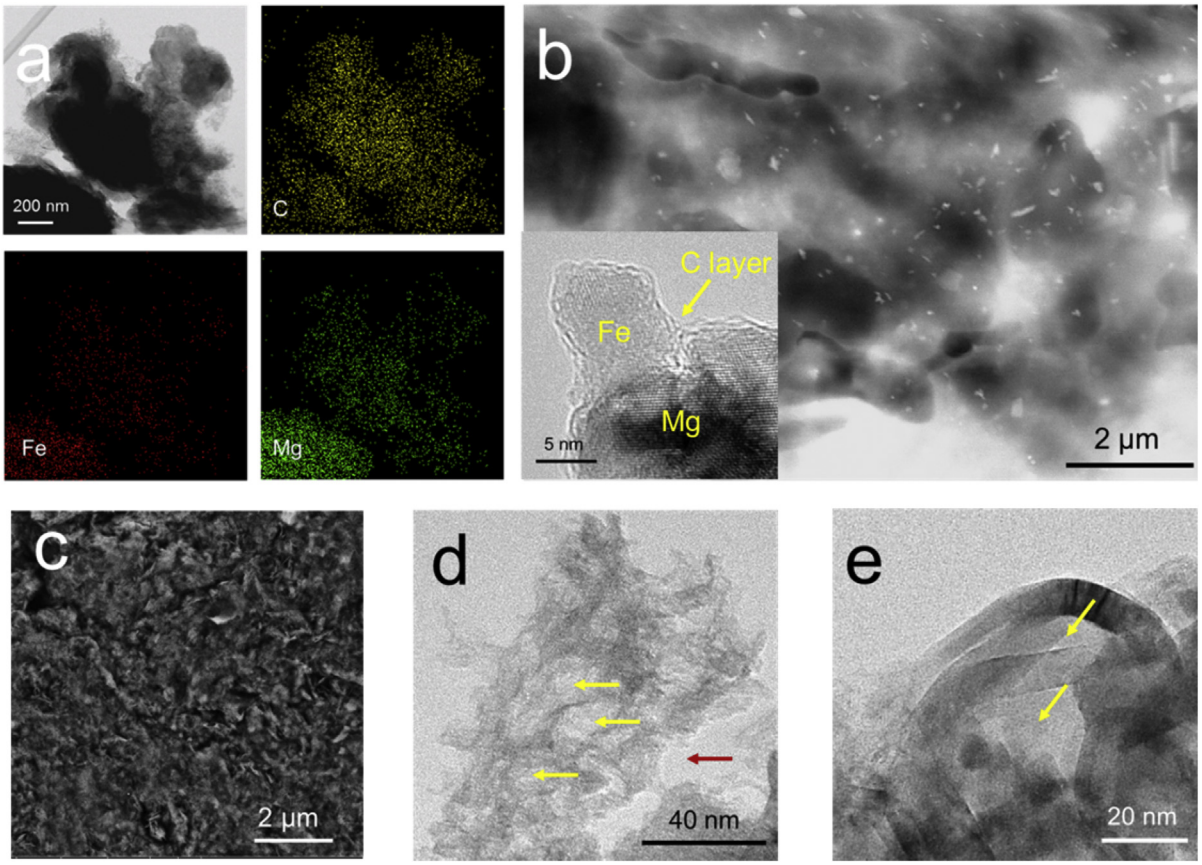

Fig. 4. (a) TEM image and EDX elemental mappings of FeMg-500; (b) SEM backscattered electron image of FeMg-900 and the HRTEM micrograph (inset) of an exsolved Fe nanoparticle on the MgO surface, encapsulated by graphitic layers. (c) SEM and (d,e) HRTEM images of FeMg-carbon. Yellow and red arrows indicate typical meso- and macropores, respectively. (A colour version of this figure can be viewed online.)

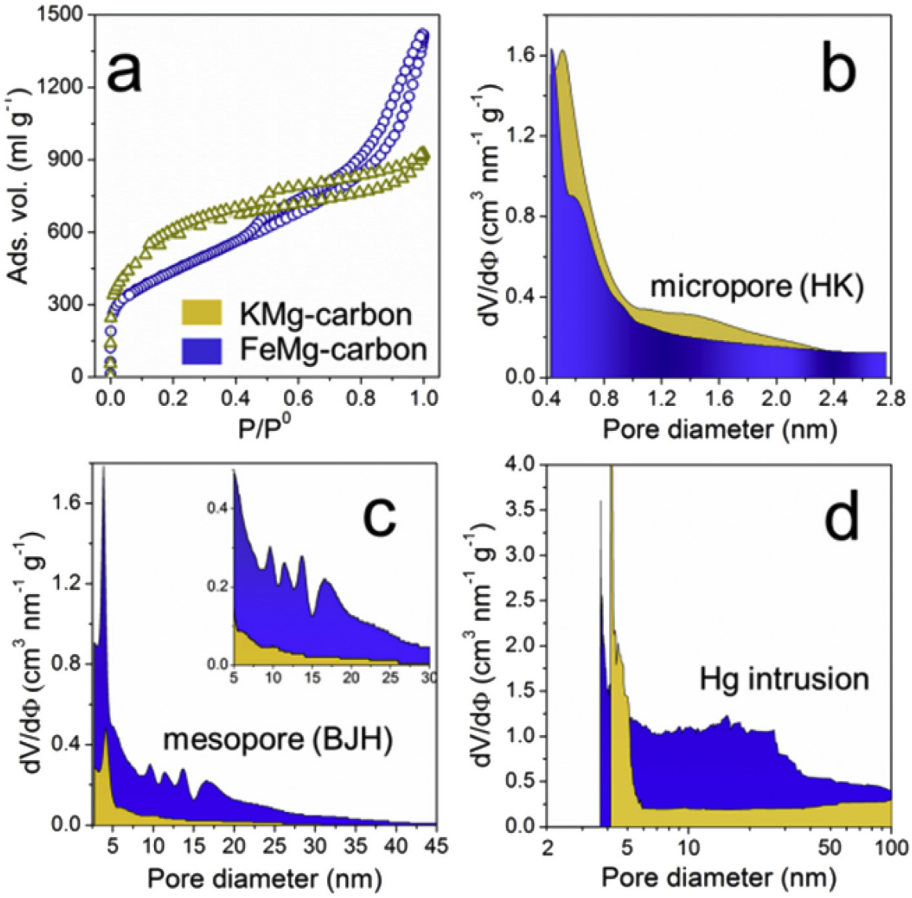

Fig. 5. (a) N_2-adsorption isotherms of KMg-carbon and FeMg-carbon at 77 K and the calculated pore size distributions using (b) Horváth–Kawazoe and (c) Barrett–Joyner–Halenda method; (d) meso- and macropore size distribution analysis using mercury intrusion porosimetry. (A colour version of this figure can be viewed online.)

from the N_2-adsorption analysis. This common discrepancy reflects the limited maximum pressure achievable during the intrusion, restricting the access of mercury atoms to the entire pore structure [36,37]. Importantly, the macropores ran through the sample, opening at both ends and forming a porous network. This was simply because the uniformly dispersed MgO templates accounted for more than 45 vol% in the FeMg-900 hybrid (see the thermogravimetric analysis in Fig. S9), way above the percolation threshold [38]. The contiguous templates guaranteed the formation of through pores. Thus, combined with the microscopic analysis results, we found that the *in-situ* exsolution of dual-template approach indeed created HPCs with interconnected pores.

Thanks to its hierarchical porous structure, the FeMg-carbon sample showed excellent electrochemical performance in oxygen reduction reaction (ORR) and supercapacitor test. The cyclic voltammograms of FeMg-carbon recorded in N_2 and O_2 saturated 0.1 M KOH electrolyte confirmed that the ORR triggered the reduction peak (see Fig. S10). We then ran linear-sweep voltammetry (LSV) at 1600 rpm for different catalysts in Fig. 6a. The hierarchically porous FeMg-carbon showed an onset potential of 0.90 V (*vs.* RHE and hereafter) and a half-wave potential of 0.77 V. The Koutecký–Levich plots indicated that the number of electron transferred was 3.5 (see LSV curves at various rotations in Fig. S11). A chronoamperometric response at the half-wave potential revealed that more than 80% of the current was sustained after 20 h measurement (see Fig. S12). All these performances herein ranked it among the best carbon ORR catalyst today (see the comparison in Table S2) [27–33,39], and were even comparable other heteroatom doped carbon materials [10,13,33,40].

Conversely, the FeMg-900 catalyst, with the pores blocked by templates, performed poorly in ORR, asserting the significant contribution of hierarchical pores in this catalytic process. This also in turns precluded the contribution of iron residuals in FeMg-carbon, if any, in ORR (note that Fe was detected by neither XPS nor Raman). Similarly, the KMg-carbon control, which possessed less interconnected hierarchical pores, was less active as well. This disparity was also prominent in the electrochemical impedance spectroscopy measurement in Fig. S13 obtained at the half-wave potentials. Besides, the lower polarization value of FeMg-carbon also indicates the faster ion movement at the electrode/electrolyte interface as a result of the interconnected pore structure. Thus, we concluded that the hierarchical pore was a key factor promoting ORR activity. Since FeMg-carbon contained much more intrinsic topological defects. The abundant carbon vacancies, edges, non-hexagonal topologies, danglings, etc., along with the nitrogen moieties also contribute greatly to the good electrocatalytic performance [33].

Its high surface area and large pore volume make the hierarchically porous FeMg-carbon an excellent candidate material for supercapacitor electrodes. To test this, we used the three-electrode configuration. The cyclic valtammetry (CV) curves in Fig. 6c are quasi-rectangular, typical of electrical double-layer capacitance (EDLC) with minor pseudo-capacitance contribution that comes from the nitrogen functionalities. The measured specific capacitance reached 321 F g^{-1} at 5 mV s^{-1}, which is comparable with top carbon electrode in the literature. Albeit that KMg-carbon had

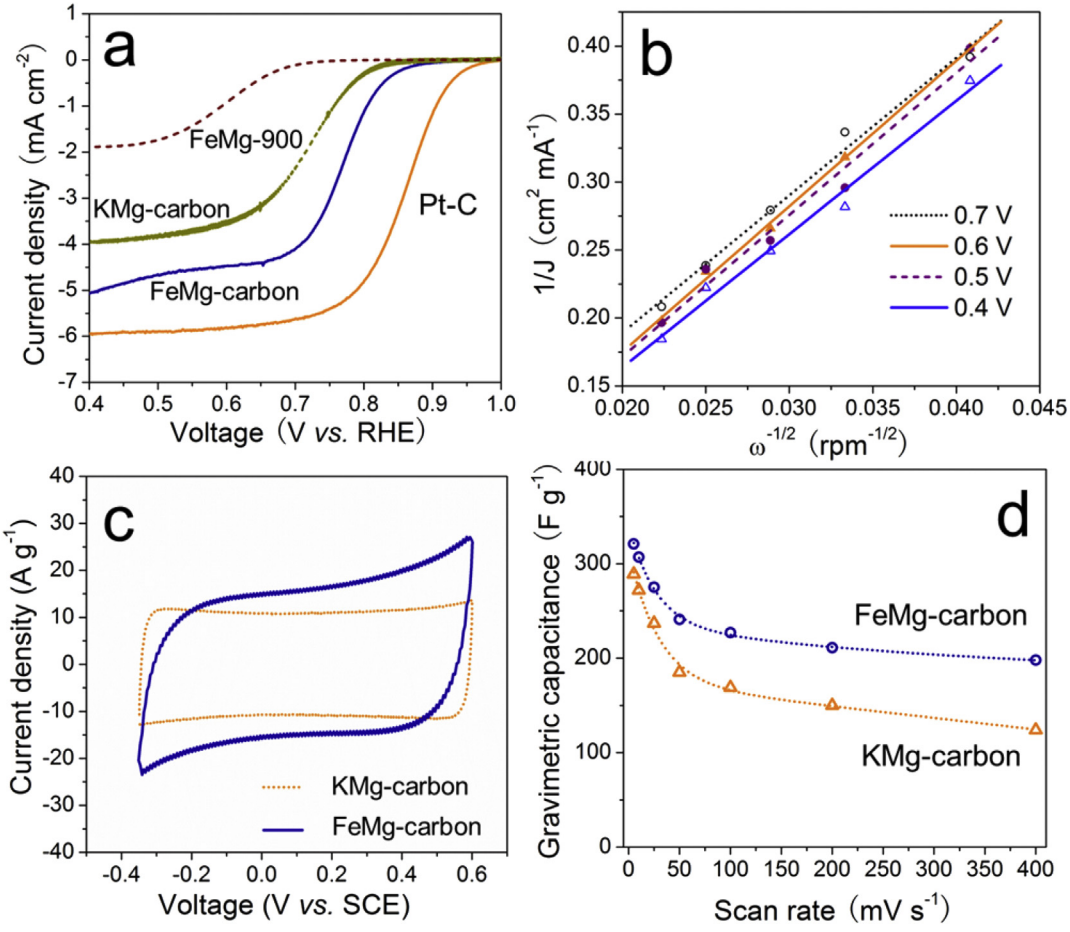

Fig. 6. (a) LSV curves of different catalysts at 1600 rpm in O_2 saturated 0.1 M KOH electrolyte; (b) The Koutecký–Levich plots of FeMg-carbon in ORR; (c) CV curves of KMg-carbon and FeMg-carbon at 50 mV s^{-1} and (d) gravimetric capacitance of KMg-carbon and FeMg-carbon at different scan rate in 1 M H_2SO_4. (A colour version of this figure can be viewed online.)

higher specific surface area, its capacitance was apparently lower than that of FeMg-carbon. This difference became much more significant when the scan rate increased till 400 mV s^{-1} in Fig. 6d, indicating that good electrolyte transportation was largely sustained in FeMg-carbon thanks to the equipped the interconnected pore structure. In fact, the surface area of the KMg-carbon mainly came from the micropore which are often poorly accessible or wholly inaccessible for the relatively larger solvated electrolyte ions [41]. In particular, pores narrower than 0.5 nm cannot support the formation of double layers [42]. Thus, high mesoporosity was always recognized as a crucial factor governing the level of EDLC. In contrast, the high surface area of FeMg-carbon largely came from the mesopores that well connected with the macropores (see Table S1). This facilitated the transportation and diffusion of electrolyte ions.

4. Conclusions

In conclusion, the *in-situ* exsolved iron-nanoparticles from the MgO offered a connected dual-template network embedded in the NTA derived N-doped carbons. It created abundant intrinsic defects and hierarchical pore structure with excellent pore interconnectivity in the carbon. Thanks to this, the resulting carbon catalyst exhibited good performances in both ORR and EDLC measurements. This approach opens new opportunities for designing porous materials with guaranteed interconnected pores, which could be useful in a variety of applications.

Acknowledgements

We thank Ing. N.J. Geels for the N_2 adsorption and mercury intrusion measurements, and the NWO-GDST Advanced Materials program (project No. 729.001.022) for support. This work is part of the Research Priority Area Sustainable Chemistry of the UvA, http://suschem.uva.nl.

Appendix A. Supplementary data

Supplementary data related to this article can be found at https://doi.org/10.1016/j.carbon.2017.12.019.

References

[1] J. Wei, D.D. Zhou, Z.K. Sun, Y.H. Deng, Y.Y. Xia, D.Y. Zhao, A controllable synthesis of rich nitrogen-doped ordered mesoporous carbon for CO_2 capture and supercapacitors, Adv. Funct. Mater. 23 (2013) 2322–2328.
[2] M. Sevilla, A.B. Fuertes, Sustainable porous carbons with a superior performance for CO_2 capture, Energy Environ. Sci. 4 (2011) 1765–1771.
[3] G. Srinivas, V. Krungleviciute, Z.-X. Guo, T. Yildirim, Exceptional CO_2 capture in a hierarchically porous carbon with simultaneous high surface area and pore volume, Energy Environ. Sci. 7 (2014) 335–342.
[4] J. Hu, M. Noked, E. Gillette, F. Han, Z. Gui, C. Wang, et al., Dual-template synthesis of ordered mesoporous carbon/Fe_2O_3 nanowires: high porosity and structural stability for supercapacitors, J. Mater. Chem. A 3 (2015) 21501–21510.
[5] S.H. Joo, S. Jun, R. Ryoo, Synthesis of ordered mesoporous carbon molecular sieves cmk-1, Microporous Mesoporous Mater. 44 (2001) 153–158.
[6] S. Dutta, A. Bhaumik, K.C.W. Wu, Hierarchically porous carbon derived from

polymers and biomass: effect of interconnected pores on energy applications, Energy Environ. Sci. 7 (2014) 3574–3592.
[7] J.-S. Wei, H. Ding, Y.-G. Wang, H.-M. Xiong, Hierarchical porous carbon materials with high capacitance derived from schiff-base networks, ACS Appl. Mater. Interfac. 7 (2015) 5811–5819.
[8] X.-Y. Yang, L.-H. Chen, Y. Li, J.C. Rooke, C. Sanchez, B.-L. Su, Hierarchically porous materials: synthesis strategies and structure design, Chem. Soc. Rev. 46 (2017) 481–558.
[9] D. Eisenberg, W. Stroek, N.J. Geels, S. Tanase, M. Ferbinteanu, S.J. Teat, et al., A rational synthesis of hierarchically porous, N-doped carbon from Mg-based MOFs: understanding the link between nitrogen content and oxygen reduction electrocatalysis, Phys. Chem. Chem. Phys. 18 (2016) 20778–20783.
[10] D. Eisenberg, W. Stroek, N.J. Geels, C.S. Sandu, A. Heller, N. Yan, et al., A simple synthesis of an n-doped carbon ORR catalyst: hierarchical micro/meso/macro porosity and graphitic shells, Chem. Eur. J. 22 (2016) 501–505.
[11] Y.J. Cai, Y. Luo, H.W. Dong, X. Zhao, Y. Xiao, Y.R. Liang, et al., Hierarchically porous carbon nanosheets derived from moringa oleifera stems as electrode material for high-performance electric double-layer capacitors, J. Power Sources 353 (2017) 260–269.
[12] Y. You, W.C. Zeng, Y.X. Yin, J. Zhang, C.P. Yang, Y.W. Zhu, et al., Hierarchically micro/mesoporous activated graphene with a large surface area for high sulfur loading in li-s batteries, J. Mater. Chem. A 3 (2015) 4799–4802.
[13] W.H. He, C.H. Jiang, J.B. Wang, L.H. Lu, High-rate oxygen electroreduction over graphitic-n species exposed on 3d hierarchically porous nitrogen-doped carbons, Angew. Chem. Int. Ed. 53 (2014) 9503–9507.
[14] K. Lehmann, O. Yurchenko, A. Heilemann, S. Vierrath, L. Zielke, S. Thiele, et al., High surface hierarchical carbon nanowalls synthesized by plasma deposition using an aromatic precursor, Carbon 118 (2017) 578–587.
[15] H. Nishihara, T. Kyotani, Templated nanocarbons for energy storage, Adv. Mater. 24 (2012) 4473–4498.
[16] S. Kyeongse, L. Youngmin, J. Mi Ru, N. Ki Min, K. Yong-Mook, Comprehensive design of carbon-encapsulated fe 3 o 4 nanocrystals and their lithium storage properties, Nanotechnology 23 (2012), 505401.
[17] Y. Liang, F. Liang, D. Wu, Z. Li, F. Xu, R. Fu, Construction of a hierarchical architecture in a wormhole-like mesostructure for enhanced mass transport, Phys. Chem. Chem. Phys. 13 (2011) 8852–8856.
[18] K.A. Cychosz, R. Guillet-Nicolas, J. Garcia-Martinez, M. Thommes, Recent advances in the textural characterization of hierarchically structured nanoporous materials, Chem. Soc. Rev. 46 (2017) 389–414.
[19] O. Kwon, S. Sengodan, K. Kim, G. Kim, H.Y. Jeong, J. Shin, et al., Exsolution trends and co-segregation aspects of self-grown catalyst nanoparticles in perovskites, Nat. Commun. 8 (2017).
[20] B. Hua, M. Li, Y.F. Sun, Y.Q. Zhang, N. Yan, J. Chen, et al., A coupling for success: controlled growth of co/coox nanoshoots on perovskite mesoporous nanofibres as high-performance trifunctional electrocatalysts in alkaline condition, Nano Energy 32 (2017) 247–254.
[21] J.R. Pels, F. Kapteijn, J.A. Moulijn, Q. Zhu, K.M. Thomas, Evolution of nitrogen functionalities in carbonaceous materials during pyrolysis, Carbon 33 (1995) 1641–1653.
[22] G. Wu, P. Zelenay, Nanostructured nonprecious metal catalysts for oxygen reduction reaction, Acc. Chem. Res. 46 (2013) 1878–1889.
[23] J. Pandey, B. Hua, W. Ng, Y. Yang, K. van der Veen, J. Chen, et al., Developing hierarchically porous MnOx/NC hybrid nanorods for oxygen reduction and evolution catalysis, Green Chem. 19 (2017) 2793–2797.
[24] S. Phokha, J. Klinkaewnarong, S. Hunpratub, K. Boonserm, E. Swatsitang, S. Maensiri, Ferromagnetism in fe-doped mgo nanoparticles, J. Mater. Sci. Mater. Electron. 27 (2016) 33–39.
[25] H. Estrade-Szwarckopf, Xps photoemission in carbonaceous materials: a "defect" peak beside the graphitic asymmetric peak, Carbon 42 (2004) 1713–1721.
[26] K. Ganesan, S. Ghosh, N. Gopala Krishna, S. Ilango, M. Kamruddin, A.K. Tyagi, A comparative study on defect estimation using XPS and Raman spectroscopy in few layer nanographitic structures, Phys. Chem. Chem. Phys. 18 (2016) 22160–22167.
[27] S. Jiang, Z. Li, H. Wang, Y. Wang, L. Meng, S. Song, Tuning nondoped carbon nanotubes to an efficient metal-free electrocatalyst for oxygen reduction reaction by localizing the orbital of the nanotubes with topological defects, Nanoscale 6 (2014) 14262–14269.
[28] Y. Jiang, L. Yang, T. Sun, J. Zhao, Z. Lyu, O. Zhuo, et al., Significant contribution of intrinsic carbon defects to oxygen reduction activity, ACS Catal. 5 (2015) 6707–6712.
[29] Y. Jia, L. Zhang, A. Du, G. Gao, J. Chen, X. Yan, et al., Defect graphene as a trifunctional catalyst for electrochemical reactions, Adv. Mater. 28 (2016) 9532–9538.
[30] X. Zhao, X. Zou, X. Yan, C.L. Brown, Z. Chen, G. Zhu, et al., Defect-driven oxygen reduction reaction (orr) of carbon without any element doping, Inorg. Chem. Front. 3 (2016) 417–421.
[31] D. Lu, D. Wu, J. Jin, L. Chen, Defect-induced catalysis toward the oxygen reduction reaction in single-walled carbon nanotube: nitrogen doped and non-nitrogen doped, Electrochim. Acta 215 (2016) 66–71.
[32] Z.J. Liu, Z.H. Zhao, Y.Y. Wang, S. Dou, D.F. Yan, D.D. Liu, et al., In situ exfoliated, edge-rich, oxygen-functionalized graphene from carbon fibers for oxygen electrocatalysis, Adv. Mater. 29 (2017), 1606207.
[33] C. Tang, Q. Zhang, Nanocarbon for oxygen reduction electrocatalysis Dopants, edges, and defects, Adv. Mater. 29 (2017) 1604103.
[34] M.H. Rümmeli, C. Kramberger, A. Grüneis, P. Ayala, T. Gemming, B. Büchner, et al., On the graphitization nature of oxides for the formation of carbon nanostructures, Chem. Mater. 19 (2007) 4105–4107.
[35] E. Thompson, A.E. Danks, L. Bourgeois, Z. Schnepp, Iron-catalyzed graphitization of biomass, Green Chem. 17 (2015) 551–556.
[36] G. Leofanti, M. Padovan, G. Tozzola, B. Venturelli, Surface area and pore texture of catalysts, Catal. Today 41 (1998) 207–219.
[37] J. Kenvin, J. Jagiello, S. Mitchell, J. Perez-Ramirez, Unified method for the total pore volume and pore size distribution of hierarchical zeolites from argon adsorption and mercury intrusion, Langmuir 31 (2015) 1242–1247.
[38] M.J. Powell, Site percolation in randomly packed spheres, Phys. Rev. B 20 (1979) 4194–4198.
[39] H. Zhao, C. Sun, Z. Jin, D.-W. Wang, X. Yan, Z. Chen, et al., Carbon for the oxygen reduction reaction: a defect mechanism, J. Mater. Chem. A 3 (2015) 11736–11739.
[40] Y. Wang, H.Y. Liu, K. Wang, S.Q. Song, P. Tsiakaras, 3d interconnected hierarchically porous n-doped carbon with NH_3 activation for efficient oxygen reduction reaction, Appl. Catal. B 210 (2017) 57–66.
[41] T. Chen, L. Dai, Carbon nanomaterials for high-performance supercapacitors, Mater. Today 16 (2013) 272–280.
[42] T.E. Rufford, D. Hulicova-Jurcakova, Z. Zhu, G.Q. Lu, Empirical analysis of the contributions of mesopores and micropores to the double-layer capacitance of carbons, J. Phys. Chem. C 113 (2009) 19335–19343.